

Physics-Based Learning of the Wave Speed Landscape in Complex Media.

Baptiste Hériard-Dubreuil^{1,*}, Emma Brenner^{1,3}, Benjamin Rio¹, William Lambert³, Foucauld Channing's², Mathias Fink¹, Alexandre Aubry^{1,*}

¹Institut Langevin, ESPCI, PSL University, CNRS, Paris, France.

²SuperSonic Imagine Company, Aix-en-Provence, France. ²Institut Bergonié, Bordeaux, France.

*Corresponding authors. Email: baptiste.hériard-dubreuil@espci.fr, alexandre.aubry@espci.fr

Wave velocity is a key parameter for imaging complex media, but in vivo measurements are typically limited to reflection geometries, where only backscattered waves from short-scale heterogeneities are accessible. As a result, conventional reflection imaging fails to recover large-scale variations of the wave velocity landscape. Here we show that matrix imaging overcomes this limitation by exploiting the quality of wave focusing as an intrinsic guide star. We model wave propagation as a trainable multi-layer network that leverages optimization and deep learning tools to infer the wave velocity distribution. We validate this approach through ultrasound experiments on tissue-mimicking phantoms and human breast tissues, demonstrating its potential for tumour detection and characterization. Our method is broadly applicable to any kind of waves and media for which a reflection matrix can be measured.

In wave imaging, the goal is to characterize an unknown medium by actively probing it and recording the waves scattered by its internal heterogeneities. Large-scale variations of the wave velocity induce wavefront distortions that can be exploited in transmission geometries to reconstruct the velocity landscape, as performed in diffraction tomography in optics (1), ultrasound (2), and

seismology (3). In contrast, most *in vivo* or *in situ* applications operate in reflection, where only backscattered echoes generated by short-scale heterogeneities are accessible. In such epi-detection configurations, recorded signals primarily encode reflectivity rather than wave velocity, yielding qualitative images that sample only a limited portion of the object's spatial frequency spectrum (4).

Recovering large-scale variations of the wave velocity from reflection data is not straightforward and often requires to go beyond the single-scattering (Born) approximation and exploit multiple scattering (5, 6, 7). This challenge has motivated the development of full waveform inversion (8), nonlinear reconstruction techniques (9, 10, 11), and learning-based approaches (12, 13). While powerful, these methods are often computationally demanding, sensitive to model mismatch, and prone to convergence issues, which limits their robustness and practical applicability.

Here we adopt a more physical approach based on reflection matrix imaging (14, 15, 16). Conventional reflection imaging relies on confocal focusing at each point to extract local reflectivity. Matrix imaging, by contrast, decouples the transmitted and received focal spots (17), yielding a focused reflection matrix that encodes the cross-talk between virtual transducers synthesized directly inside the medium. This representation provides access to the quality of wave focusing itself, and thus to the wavefront distortions accumulated during propagation (17, 18, 16). These distortions arise from discrepancies between the true wave velocity distribution and the background model used for focusing. While previous studies have shown that such distortions can be inverted to estimate velocity maps, they typically rely on restrictive assumptions such as straight-ray propagation (19, 20) or simplified geometries (21, 22).

In this work, we introduce a learning-based formulation of matrix imaging that exploits the quality of wave focusing as an intrinsic guide star. We model wave propagation as a differentiable multi-layer forward model based on cascaded diffraction phase screens (23, 24) interleaved with free-space propagation (25, 26). This representation enables the use of gradient-based optimization to iteratively recover the wave velocity landscape from reflection data alone. We validate this approach through ultrasound experiments on tissue-mimicking phantoms, *ex vivo* tissues, and human breast data, demonstrating quantitative speed-of-sound imaging in reflection geometry. The proposed framework is general and can be applied to any wave modality for which a reflection matrix can be measured.

Matrix Imaging as a Versatile Framework

Matrix imaging begins with the acquisition of a reflection matrix by sequentially transmitting incident wavefronts into the medium and recording the backscattered signals on an array of sensors (Materials and Methods, Fig. 1A). The measured data form a time-dependent reflection matrix $\mathbf{R}_{io}(t) = [\mathcal{R}(\mathbf{u}_{in}, \mathbf{u}_{out}, t)]$, whose elements encode the impulse responses between each source/receiver pair identified by their position $\mathbf{u}_{in/out}$. Under a single backscattering approximation, this matrix can be expressed in the frequency domain as an integral over the medium reflectivity $\gamma(\mathbf{r})$ convolved by Green's functions $\mathcal{G}(\mathbf{u}, \mathbf{r}, f)$ that account for wave propagation through the large-scale velocity distribution:

$$\mathcal{R}(\mathbf{u}_{in}, \mathbf{u}_{out}, f) = \int d\mathbf{r} \mathcal{G}(\mathbf{u}_{in}, \mathbf{r}, f) \gamma(\mathbf{r}) \mathcal{G}(\mathbf{u}_{out}, \mathbf{r}, f). \quad (1)$$

To form an image, the recorded signals are numerically focused at depth using an estimate of the Green's matrix, $\mathbf{T}_{xi/o}(z, f; c) = [\mathcal{T}(\mathbf{x}, \mathbf{u}, z, f; c)]$, derived from a trial velocity distribution $c(\mathbf{r})$:

$$\overline{\mathbf{R}}_{xx}(z; c) = \sum_f \mathbf{T}_{xi}^*(z, f; c) \times \mathbf{R}_{io}(f) \times \mathbf{T}_{xo}^\dagger(z, f; c). \quad (2)$$

The symbols \times , $*$ and \dagger stand for matrix product, conjugate, conjugate transpose, respectively. This operation yields focused reflection matrices $\overline{\mathbf{R}}_{xx}(z; c)$ (Fig. 1D), whose diagonal elements correspond to confocal signals conventionally used to estimate reflectivity (Fig. 1E). Importantly, the off-diagonal structure of these matrices provides additional information: the spreading of backscattered energy away from the diagonal directly reflects wavefront distortions induced by velocity mismatches.

This property allows us to define a focusing quality metric that quantifies the efficiency of numerical focusing at each depth. Specifically, we compute the ratio \mathcal{F} between the average confocal energy and the total backscattered energy in $\overline{\mathbf{R}}_{xx}(z; c)$ (Fig. 1F):

$$\mathcal{F}(c) = \left\langle \frac{|\overline{\mathcal{R}}(\mathbf{x}, \mathbf{x}, z; c)|^2}{\sum_{\mathbf{x}'} |\overline{\mathcal{R}}(\mathbf{x}', \mathbf{x}, z; c)|^2} \right\rangle_{\mathbf{x}, z}. \quad (3)$$

The symbol $\langle \dots \rangle$ stands for an average over the variables in subscript. This dimensionless quantity serves as a physically meaningful indicator of model adequacy: when the velocity model matches the true medium, focusing is optimal and the metric is maximized.

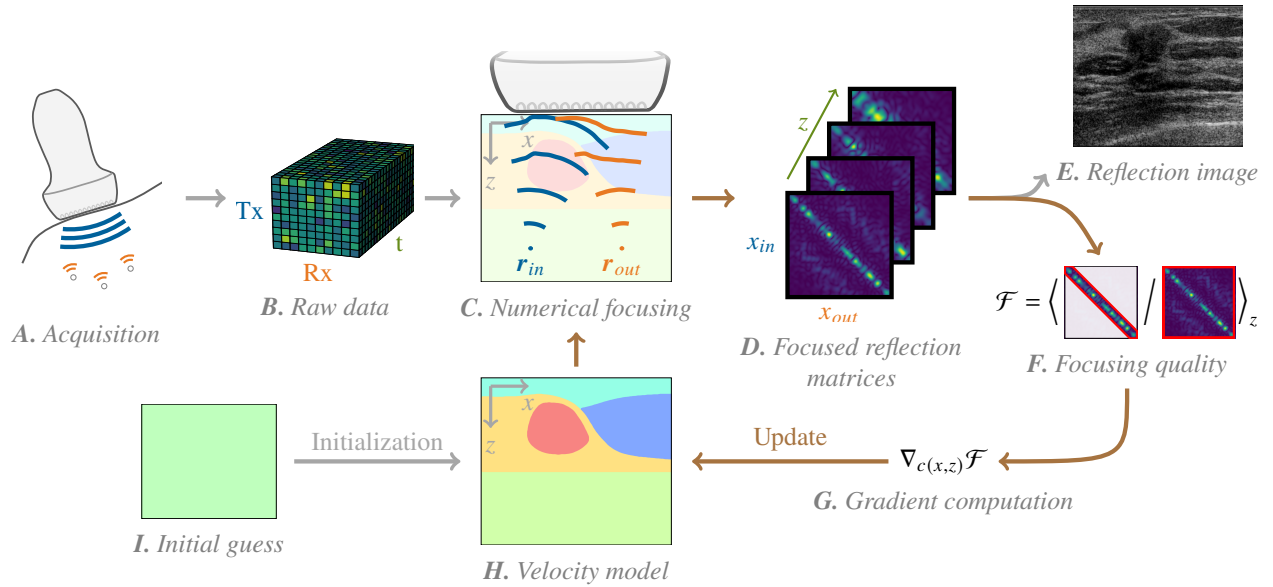


Figure 1: Differential matrix imaging. **(A)** an ultrasound acquisition is performed with an ultrasound probe. **(B)** Raw data is gathered in a 3D tensor, indexed by emission (**Tx**), reception (**Rx**) and time (**t**). **(C)** A numerical focusing algorithm focuses the signals at point r_{in} in emission and r_{out} in reception according to a velocity model (**H**). **(D)** The repetition of this operation for different depths and lateral positions yields focused reflection matrices. From these matrices, we obtain either **(E)** a reflection image or **(F)** a focusing quality computed by averaging the energy on the diagonal, divided by the total energy of reflection matrices. **(G)** The focusing quality gradient with respect to the velocity model is then computed to update the current velocity model, in a gradient ascent scheme. **(I)** An initial guess of the velocity model (often chosen as uniform) is required to start the optimization process.

Combining Wave Physics and Optimization

Rather than performing an exhaustive search over velocity models, we exploit the differentiability of the focusing process to perform a gradient ascent of the focusing quality with respect to the velocity distribution (brown loop in Fig. 1). To do so, we can compute its derivative using the chain rule:

$$\nabla_c \mathcal{F}(c) = \sum_z \frac{\partial \mathcal{F}(c)}{\partial \bar{\mathbf{R}}_{xx}(z; c)} \cdot \frac{\partial \bar{\mathbf{R}}_{xx}(z; c)}{\partial c}. \quad (4)$$

This derivative indicates the direction in which updating the velocity map would result in the highest increase of the focusing quality. This formulation transforms wave velocity estimation into an optimization problem driven by an intrinsic, data-derived loss function, without requiring access to transmission measurements or prior knowledge of short-scale disorder.

The gradient-ascent framework is highly flexible, as each block in Fig. 1 can be implemented by any fully differentiable operator. This allows the incorporation of advanced focusing strategies that account for refraction, diffraction, and forward multiple scattering. Here, we adopt a forward model based on the split-step Fourier method used in geophysics (25, 26), also known as the beam propagation method in optics (27) (Materials and methods). Wave propagation is described as a sequence of diffraction phase screens capturing lateral refractive-index fluctuations, $\delta n(x, z) = n(x, z) - \bar{n}(z)$, interleaved with free-space propagation governed by the laterally-averaged refractive index $\bar{n}(z) = \langle n(x, z) \rangle_x$ (Fig. 2), with $n(x, z) = c_0/c(x, z)$.

Thanks to this architecture, our approach can actually be reformulated as a self-supervised learning problem. On the one hand, the focusing quality function plays the role of a loss. On the other hand, the numerical focusing process can be expressed as a multi-layer network made of a succession of elementary operations analogous to neural layers. Their weights are dictated by diffraction and the activation functions are parameterized by the local wave velocity. We can therefore benefit from the development of resources dedicated to the implementation and training of deep neural network. These resources include auto-differentiable languages (e.g. PyTorch (28), JAX (29)) designed for the gradient-descent-based training of neural networks. Such languages combine Python’s efficient prototyping with built-in optimization features, automatic differentiation and GPU-based accelerations.

To encompass a wide range of heterogeneous media, we use a large number of phase screens

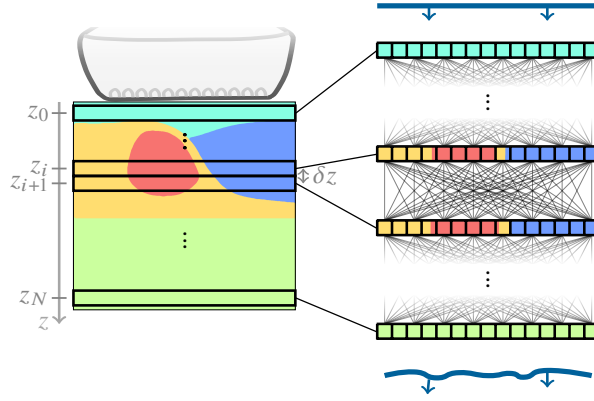


Figure 2: Multi-layer network as a forward model. The propagation of incident and reflected waves is modelled as a succession of diffraction phase screens, $\exp [j2\pi f\delta n(x, z_i)\delta z/c_0]$, and free-space operators $\mathbf{T}(\delta z, f; c_0/\bar{n}(z_i))$ in homogeneous layers of thickness δz and refractive index $\bar{n}(z_i)$. This forward model takes the form of a multi-layer network.

(typically one par wavelength), and optimize them all simultaneously. The resulting high dimensional problem is ill-posed and strongly non-linear, rising several convergence issues. We overcome such challenges by leveraging optimization techniques like total-variation regularization (30), spatial filtering, variable splitting and Lagrangian relaxation (see Materials and methods). The whole post-processing pipeline (Materials and Methods) and hyper-parameters (Table S1) have been tuned and validated by means of numerical simulations described in the Supplementary Text.

Focusing Quality as a Guide Star

Ultrasound imaging offers a convenient and versatile platform to demonstrate our approach. Using transducer arrays, the reflection matrix can be readily measured by emitting broadband pulses and recording the reflected wave fields with wavelength-scale spatial sampling (Fig. 1A; Materials and Methods). Soft biological tissues are particularly well suited to this framework, as they combine a random distribution of unresolved scatterers and pronounced sound-speed variations across tissue types such as fat, skin, and muscle (31).

As a proof of concept, we apply our approach to open ultrasound data from a 2D in vitro experiment (32) (Fig. 3A). The tissue-mimicking phantom generates random speckle and contains shallow sound-speed inclusions ($z \sim 10$ mm), deep anechoic regions ($z \sim 40$ mm), and intermediate-depth

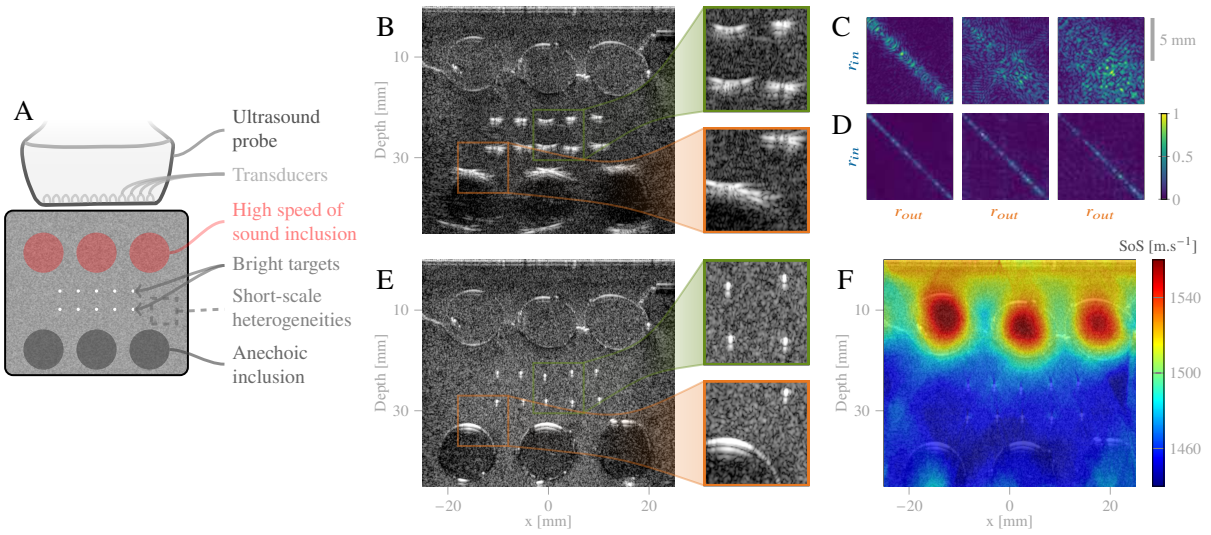


Figure 3: Ultrasound aberration correction and speed of sound imaging in a 2D *in vitro* experiment. Data obtained from (32). (A) Experiment performed in (32), in which an ultrasound probe is positioned on top of a homemade tissue-mimicking phantom with speed of sound inclusions. (B) Aberrated reflection image obtained with a uniform speed of sound hypothesis of $c = 1480 \text{ m.s}^{-1}$. Two zoomed sections are displayed on the right. The dynamic range of the B&W scale is of 50 dB. (C) Examples of focused reflection matrices obtained at initialization and (D) at convergence, at depths of 20 mm, 30 mm and 40 mm, normalized by their maximum. (E) Corrected reflection image obtained at convergence with the speed of sound map displayed in panel F (see Movie S1). (F) Obtained speed of sound map (overlaid on the corrected reflection image), color coded as a function of the speed of sound expressed in m.s^{-1} .

nylon rods acting as point scatterers. A conventional image beamformed with a homogeneous sound speed ($c_0 = 1480 \text{ m.s}^{-1}$) is shown in Fig. 3B.

Sound-speed heterogeneities induce strong aberrations, visible as distortions of point reflectors and deformations of anechoic interfaces, and as a progressive off-diagonal spreading of the focused reflection matrices with depth (Fig. 3C). This behavior is quantitatively captured by the focusing-quality metric $\mathcal{F}(c)$ (Eq. 3), which is used to derive the differential matrix imaging (DMI) optimization (Fig. 1). The resulting sound-speed map (Fig. 3F) accurately recovers the expected structure, with well-resolved inclusions exhibiting a $\sim 100 \text{ m.s}^{-1}$ contrast, outperforming previous approaches (20, 33).

After correction, the reflection matrices collapse onto their diagonals (Fig. 3D), indicating diffraction-limited focusing. The corresponding confocal images (Fig. 3E) resolve individual point-like scatterers and restore the circular geometry of anechoic regions, demonstrating the benefit of an optimized sound-speed model for reflectivity imaging.

From 2D to 3D Ex Vivo Imaging

To demonstrate the extension of our framework to three-dimensional imaging, we apply the method to a 3D in vitro experiment (16). A matrix transducer array images a tissue-mimicking phantom placed behind a layer of pork tissue composed of fat and muscle (Fig. 4). While the conventional ultrasound image fails to distinguish these layers (Fig. 4B, Movie S2), the overlying tissue acts as a strong aberrator. This effect is revealed by the reflection point spread functions (RPSFs) extracted from the antidiagonals of $\mathbf{R}_{xx}(z)$ (Fig. 4C), which display a distorted confocal peak superimposed on a diffuse background arising from multiple scattering. These distortions are again captured by the focusing metric $\mathcal{F}(c)$.

We apply the DMI optimization to the corresponding open-access dataset (34). To accommodate the large data volume, we factorize the forward model and batch frequency components during gradient computation (Materials and Methods). The converged 3D sound-speed map (Fig. 4D) clearly discriminates fat ($c \sim 1520 \text{ m.s}^{-1}$) from muscle ($c \sim 1560 \text{ m.s}^{-1}$). It perfectly matches with the distribution of muscle and fat in the pork tissue layer. Horizontal slices (Fig. 4E) highlight the lateral resolution and the uniformity of the recovered velocity beyond $z = 15 \text{ mm}$.

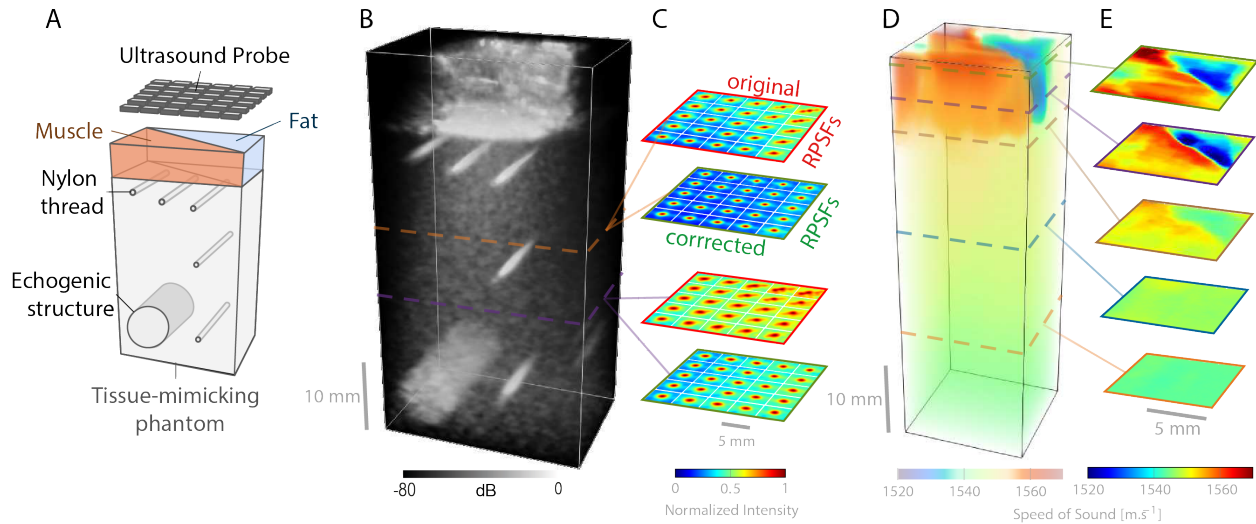


Figure 4: Speed of sound imaging of *ex vivo* tissues in a 3D configuration. Experiment performed in (16) by imaging a tissue mimicking phantom through muscle and fat with a 1024 transducers matrix probe. Data available at (34). **(A)** Drawing of the experiment performed in (16). **(B)** Corrected reflection image obtained with the 3D speed of sound map displayed in **D**. **(C)** Examples of focal spots estimated with the focused reflection matrices, at initialization (red) and after correction (green), for depths $z = 30$ mm and 40 mm. **(D)** Obtained 3D speed of sound map, color coded as a function of the speed of sound (in m.s^{-1}). **(E)** Horizontal slices of the 3D speed of sound map, at 5 mm, 10 mm, 15 mm, 30 mm and 45 mm. The speed of sound is displayed in m.s^{-1} .

Correction with the optimized sound-speed model restores a diffraction-limited confocal focus (Fig. 4C), with improved contrast relative to the diffuse background. Residual multiple scattering persists, however, underscoring the limits of the current forward model. While the multilayer network captures forward multiple-scattering effects associated with long-range sound-speed fluctuations, it does not account for more complex paths induced by short-scale heterogeneities. Addressing these effects would require more advanced models, such as Born-series approaches (7), at the cost of increased sensitivity to convergence and local minima.

Towards In Vivo Applications

Ultrasound imaging is a noninvasive, portable, real-time, and cost-effective modality widely used in clinical practice, including detection and characterization of breast lesions. However, conven-

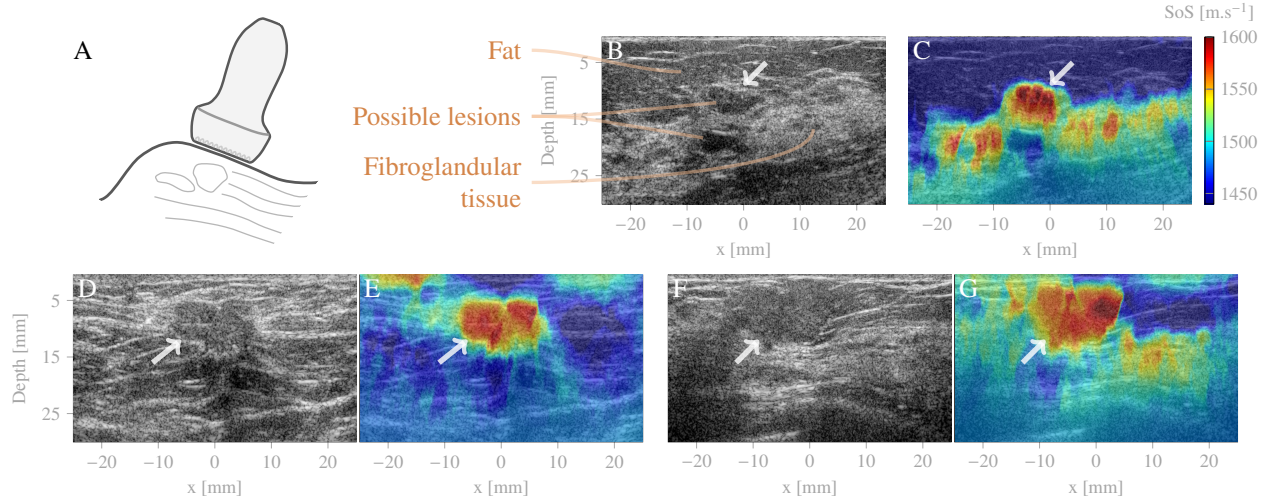


Figure 5: Sound speed imaging applied to breast ultrasound. (A) Schematic drawing of the acquisition, in which an ultrasound probe is positioned on top of breast tissues. (B, D, F, H, J) Example of reflection images obtained after correction (see Movies S3-S7 for comparison between initial and corrected images). The dynamic range of the B&W scale is of 55 dB. (C, E, G, I, K) Estimated sound speed maps overlaid on the associated reflection images. Speed of sound maps are color-coded from 1420 m.s^{-1} (blue) to 1600 m.s^{-1} (red). White arrows indicate on each image invasive carcinoma (malignant) while orange arrows correspond to benign masses.

tional B-mode images provide primarily qualitative information and require expert interpretation. Although quantitative ultrasound metrics such as shear-wave velocity have been introduced (35), their clinical adoption remains limited by hardware complexity, resolution constraints, and operator dependence.

In this context, the longitudinal wave speed is a promising parameter for tissue characterization like breast lesions assessment (33, 36). We performed a retrospective analysis of anonymized data acquired during routine breast ultrasound examinations at Institut Bergonié (Bordeaux, France). Representative B-mode images and the corresponding speed-of-sound maps obtained with DMI are shown in Fig. 5. In all cases, the recovered wave-speed distributions closely match anatomical features and enable clear differentiation between tissue types. Fat exhibits low sound speed ($\sim 1450 \text{ m.s}^{-1}$), benign mass and fibroglandular tissue intermediate values ($\sim 1525 \text{ m.s}^{-1}$ and $\sim 1550 \text{ m.s}^{-1}$, respectively), and malignant masses markedly higher speeds ($\sim 1585 \text{ m.s}^{-1}$; white arrows). Importantly, sound-speed contrast improves lesion discrimination beyond B-mode imaging alone,

as illustrated by anechoic regions that are indistinguishable in B-mode (Fig. 5B) but separable based on their wave speed (Fig. 5C).

Furthermore, by compensating for aberrations, the resulting speed-of-sound maps reveal bright point-like scatterers (Movie S7) that correspond to micro-calcifications in the reflection image (Fig. 5J). As precursors to breast cancer, these structures are vital for clinical diagnosis; however, they often remain undetected in conventional ultrasound due to aberrations induced by wave speed variations.

These findings provide a promising preliminary validation of DMI under clinical conditions for breast lesion detection and assessment. Prospective studies are required to establish sound speed as a reliable biomarker for tumor characterization. If confirmed, this approach could support ultrasound-assisted breast cancer diagnosis by reducing unnecessary biopsies and false-negative findings.

More broadly, sound speed is a versatile biomarker relevant to numerous applications, including liver disease assessment (37,38) and nondestructive testing (39). Because it reflects tissue composition, mechanical properties, and intensive parameters such as temperature or pressure, sound-speed imaging offers a general quantitative probe for monitoring biological and physical systems.

Discussion

This work demonstrates that learning-based formulations of wave propagation provide a powerful and general framework for quantitative imaging in complex media. By casting wave imaging as an optimization problem guided by a physically meaningful focusing quality metric, and by implementing the forward propagation as a multi-layer differentiable model, we bridge wave physics and modern optimization strategies in a unified framework. Rather than replacing physical modeling, our approach embeds it at the core of the learning process, enabling quantitative imaging in reflection geometries that have long been considered ill-posed.

From an inverse-problem perspective, the proposed strategy shares conceptual similarities with full-waveform inversion in seismology (8) and learning-based reconstruction techniques developed in optics (9, 12). These approaches rely on accurate forward models and data-fidelity losses defined in the measurement space, often requiring detailed prior knowledge of the medium, sources, or

initial velocity models. By contrast, our method is driven by a loss function derived from the quality of numerical focusing itself. This choice relaxes the need for detailed short-scale knowledge of the medium and enables velocity estimation directly from reflection data.

The forward model considered here relies on a multi-layer phase-screen representation that captures forward multiple scattering induced by large-scale velocity variations. This approximation is valid as long as the penetration depth remains below the transport mean free path, over which waves retain a directional memory. Beyond this regime, wave propagation becomes diffusive and involves complex scattering trajectories, as encountered for instance in optical microscopy. Extending the present framework to such a regime remains challenging, but recent developments based on multi-layer Born approximations and modified Born series (10, 40) suggest promising routes toward tractable models of diffuse multiple scattering.

DMI provides a natural level of interpretability that is often lacking in purely data-driven methods. It allows us to identify the fundamental limitations of the reconstruction process and to devise targeted mitigation strategies, such as confocal filtering or regularization schemes that stabilize convergence. At the same time, the differentiable formulation of wave propagation enables the use of modern computational tools developed for deep learning, including automatic differentiation, GPU acceleration, and scalable optimization algorithms.

The range of potential applications for DMI extends well beyond ultrasound. In optical microscopy, reflection matrix approaches have already demonstrated their ability to image biological tissues in depth (14, 18). Because speckle is ubiquitous in such media, DMI could retrieve the refractive index distribution in epi-detection. In seismology, DMI could enable high-resolution velocity tomography of scattering environments such as fault zones or volcanic edifices (41), complementing surface-wave methods and providing access to both compressional and shear wave velocities at an unprecedented resolution.

Several challenges remain. Accounting for the vectorial nature of electromagnetic or elastic waves will increase computational complexity but will also unlock access to additional physical observables, such as birefringence (42) or elastic anisotropy (43). More broadly, wave velocity is only one among other parameters governing wave propagation. The flexibility of the proposed framework makes it naturally extendable to the estimation of other material properties, including density and compressibility in acoustics or permittivity and permeability in electromagnetism.

Altogether, this work establishes learning-based matrix imaging as a unifying paradigm that combines physical insight, computational efficiency, and experimental accessibility. By exploiting reflection matrices and intrinsic focusing metrics, it opens new avenues for quantitative wave imaging across scales and modalities, in regimes that have long resisted conventional inversion strategies.

References and Notes

1. E. Wolf, Three-dimensional structure determination of semi-transparent objects from holographic data. *Opt. Commun.* **1**, 153–156 (1969).
2. A. Devaney, A filtered backpropagation algorithm for diffraction tomography. *Ultrason. Imaging* **4**, 336–350 (1982).
3. C. Thurber, J. Ritsema, *Theory and Observations - Seismic Tomography and Inverse Methods* (Elsevier, 2015), pp. 307–337.
4. A. Sentenac, J. Mertz, Unified description of three-dimensional optical diffraction microscopy: from transmission microscopy to optical coherence tomography: tutorial. *J. Opt. Soc. Am. A* **35**, 748 (2018).
5. P. Mora, *Inversion=migration+tomography* (Springer Berlin Heidelberg, 1989), pp. 78–101.
6. T. D. Weber, N. Khetan, R. Yang, J. Mertz, Ultrasound differential phase contrast using backscattering and the memory effect. *Appl. Phys. Lett.* **118**, 124103 (2021).
7. T. Wasik, V. Barolle, A. Aubry, J. Garnier, Taking advantage of multiple scattering for optical reflection tomography. *IEEE Trans. Comput. Imaging (to be published)* (2026).
8. J. Virieux, S. Operto, An overview of full-waveform inversion in exploration geophysics. *Geophysics* **74**, WCC1–WCC26 (2009).
9. U. S. Kamilov, I. N. Papadopoulos, M. H. Shoreh, A. Goy, C. Vonesch, M. Unser, D. Psaltis, Optical tomographic image reconstruction based on beam propagation and sparse regularization. *IEEE Trans. Comput. Imag.* **2**, 59–70 (2016).
10. M. Chen, D. Ren, H.-Y. Liu, S. Chowdhury, L. Waller, Multi-layer born multiple-scattering model for 3d phase microscopy. *Optica* **7**, 394–403 (2020).
11. T. Li, J. Zhu, Y. Shen, L. Tian, Reflection-mode diffraction tomography of multiple-scattering samples on a reflective substrate from intensity images. *Optica* **12**, 406 (2025).

12. U. S. Kamilov, I. N. Papadopoulos, M. H. Shoreh, A. Goy, C. Vonesch, M. Unser, D. Psaltis, Learning approach to optical tomography. *Optica* **2**, 517–522 (2015).
13. W. A. Simson, M. Paschali, V. Sideri-Lampretsa, N. Navab, J. J. Dahl, Investigating pulse-echo sound speed estimation in breast ultrasound with deep learning. *Ultrasonics* **137**, 107179 (2024).
14. S. Yoon, M. Kim, M. Jang, Y. Choi, W. Choi, S. Kang, W. Choi, Deep optical imaging within complex scattering media. *Nat. Rev. Phys.* **2**, 141–158 (2020).
15. A. Badon, V. Barolle, K. Irsch, A. C. Boccara, M. Fink, A. Aubry, Distortion matrix concept for deep optical imaging in scattering media. *Sci. Adv.* **6**, aay7170 (2020).
16. F. Bureau, J. Robin, A. Le Ber, W. Lambert, M. Fink, A. Aubry, Three-dimensional ultrasound matrix imaging. *Nat. Commun.* **14**, 6793 (2023).
17. W. Lambert, L. A. Cobus, M. Couade, M. Fink, A. Aubry, Reflection matrix approach for quantitative imaging of scattering media. *Phys. Rev. X* **10**, 021048 (2020).
18. U. Najar, V. Barolle, P. Balondrade, M. Fink, A. C. Boccara, M. Fink, A. Aubry, Harnessing forward multiple scattering for optical imaging deep inside an opaque medium. *Nat. Commun.* **15**, 7349 (2024).
19. P. Stähli, M. Kuriakose, M. Frenz, M. Jaeger, Improved forward model for quantitative pulse-echo speed-of-sound imaging. *Ultrasonics* **108**, 106168 (2020).
20. W. Simson, L. Zhuang, B. N. Frey, S. J. Sanabria, J. J. Dahl, D. Hyun, Ultrasound autofocusing: Common midpoint phase error optimization via differentiable beamforming. *IEEE Trans. Med. Imaging* (2025).
21. R. Ali, A. V. Telichko, H. Wang, U. K. Sukumar, J. G. Vilches-Moure, R. Paulmurugan, J. J. Dahl, Local sound speed estimation for pulse-echo ultrasound in layered media. *IEEE Trans. Ultrason. Ferroelectr. Freq. Control* **69**, 500–511 (2021).

22. B. Hériard-Dubreuil, A. Besson, F. Wintzenrieth, C. Cohen-Bacrie, J.-P. Thiran, Refraction-based speed of sound estimation in layered media: An angular approach. *IEEE Trans. Ultrason. Ferroelectr. Freq. Control* **70**, 486–497 (2023).
23. S. Kang, Y. Kwon, H. Lee, S. Kim, J. H. Hong, S. Yoon, W. Choi, Tracing multiple scattering trajectories for deep optical imaging in scattering media. *Nat. Commun.* **14**, 6871 (2023).
24. O. Haim, J. Boger-Lombard, O. Katz, Image-guided computational holographic wavefront shaping. *Nat. Photonics* **19**, 44–53 (2024).
25. R. H. Hardin, Applications of the split-step fourier method to the numerical solution of nonlinear and variable coefficient wave equations. *Siam Rev.* **15**, 423 (1973).
26. P. L. Stoffa, J. T. Fokkema, R. M. De Luna Freire, W. P. Kessinger, Split?step Fourier migration. *GEOPHYSICS* **55**, 410–421 (1990).
27. M. Feit, J. Fleck Jr, Light propagation in graded-index optical fibers. *Appl. Opt.* **17**, 3990–3998 (1978).
28. A. Paszke, S. Gross, F. Massa, A. Lerer, J. Bradbury, G. Chanan, T. Killeen, Z. Lin, N. Gimelshein, L. Antiga, *et al.*, Pytorch: An imperative style, high-performance deep learning library. *Adv. Neural Inf. Process. Syst.* **32** (2019).
29. S. Schoenholz, E. D. Cubuk, Jax md: a framework for differentiable physics. *Adv. Neural Inf. Process. Syst.* **33**, 11428–11441 (2020).
30. L. I. Rudin, S. Osher, E. Fatemi, Nonlinear total variation based noise removal algorithms. *Phys. D: Nonlinear Phenom.* **60**, 259–268 (1992).
31. F. A. Duck, *Acoustic Properties of Tissue at Ultrasonic Frequencies* (Elsevier, 1990), pp. 73–135.
32. R. Ali, T. M. Mitcham, M. Singh, M. M. Dooley, R. R. Bouchard, J. J. Dahl, N. Duric, Sound speed estimation for distributed aberration correction in laterally varying media. *IEEE Trans. Comput. Imaging* **9**, 367–382 (2023).

33. D. Schweizer, M. Farkas, C. D. Bezdek, A. Potempa, C. Leo, R. A. Kubik-Huch, O. Goksel, Pulse-echo imaging of breast speed of sound as a potential biomarker for breast cancer. *Ultrasound Med. Biol.* **51**, 1831–1839 (2025).

34. F. Bureau, J. Robin, A. Le Ber, W. Lambert, M. Fink, A. Aubry, Three-dimensional ultrasound matrix imaging [data set], Zenodo (2023).

35. J. Bercoff, S. Chaffai, M. Tanter, L. Sandrin, S. Catheline, M. Fink, J. Gennisson, M. Meunier, In vivo breast tumor detection using transient elastography. *Ultrasound Med. Biol.* **29**, 1387–1396 (2003).

36. C. Li, N. Duric, P. Littrup, L. Huang, In vivo breast sound-speed imaging with ultrasound tomography. *Ultrasound Med. Biol.* **35**, 1615–1628 (2009).

37. M. Imbault, A. Faccinetto, B.-F. Osmanski, A. Tissier, T. Deffieux, J.-L. Gennisson, V. Vilgrain, M. Tanter, Robust sound speed estimation for ultrasound-based hepatic steatosis assessment. *Phys. Med. Biol.* **62**, 3582 (2017).

38. P. Stähli, C. Becchetti, N. Korta Martiartu, A. Berzigotti, M. Frenz, M. Jaeger, First-in-human diagnostic study of hepatic steatosis with computed ultrasound tomography in echo mode. *Commun. Med.* **3**, 176 (2023).

39. B. Lan, M. Lowe, F. Dunne, Experimental and computational studies of ultrasound wave propagation in hexagonal close-packed polycrystals for texture detection. *Acta Materialia* **63**, 107–122 (2014).

40. G. Osnabrugge, S. Leedumrongwatthanakun, I. M. Vellekoop, A convergent born series for solving the inhomogeneous helmholtz equation in arbitrarily large media. *J. Comput. Phys.* **322**, 113–124 (2016).

41. E. Giraudat, A. Burtin, A. Le Ber, M. Fink, J.-C. Komorowski, A. Aubry, Matrix imaging as a tool for high-resolution monitoring of deep volcanic plumbing systems with seismic noise. *Commun. Earth Environ.* **5**, 509 (2024).

42. M. Villiger, D. Lorenser, R. A. McLaughlin, B. C. Quirk, R. W. Kirk, B. E. Bouma, D. D. Sampson, Deep tissue volume imaging of birefringence through fibre-optic needle probes for the delineation of breast tumour. *Sci. Rep.* **6**, 28771 (2016).

43. S. I. Ranganathan, M. Ostoja-Starzewski, Universal elastic anisotropy index. *Phys. Rev. Lett.* **101**, 055504 (2008).

44. G. Montaldo, M. Tanter, J. Bercoff, N. Benech, M. Fink, Coherent plane-wave compounding for very high frame rate ultrasonography and transient elastography. *IEEE Trans. Ultras. Ferroel. Freq. Cont.* **56**, 489–506 (2009).

45. P. Balondrade, V. Barolle, N. Guigui, E. Auriant, N. Rougier, C. Boccara, M. Fink, A. Aubry, Multi-spectral reflection matrix for ultrafast 3d label-free microscopy. *Nat. Photonics* **18**, 1097–1104 (2024).

46. W. Simson, L. Zhuang, S. J. Sanabria, N. Antil, J. J. Dahl, D. Hyun, *International Conference on Medical Image Computing and Computer-Assisted Intervention* (Springer, 2023), pp. 428–437.

47. B. Hériard-Dubreuil, A. Besson, C. Cohen-Bacrie, J.-P. Thiran, A path-based model for aberration correction in ultrasound imaging. *IEEE Trans. Med. Imaging* **44**, 3222–3232 (2025).

48. W. Lambert, L. A. Cobus, J. Robin, M. Fink, A. Aubry, Ultrasound matrix imaging—part ii: The distortion matrix for aberration correction over multiple isoplanatic patches. *IEEE Trans. Med. Imaging* **41**, 3921–3938 (2022).

49. R. Mallart, M. Fink, Adaptive focusing in scattering media through sound-speed inhomogeneities: The van cittert zernike approach and focusing criterion. *J. Acoust. Soc. Am.* **96**, 3721–3732 (1994).

50. J. Spainhour, K. Smart, S. Becker, N. Bottenus, Optimization of array encoding for ultrasound imaging. *Phys. Med. Biol.* **69**, 125024 (2024).

51. J. Garnier, L. Giovangigli, Q. Goepfert, P. Millien, Probing the speckle to estimate the effective speed of sound, a first step towards quantitative ultrasound imaging. *arXiv preprint arXiv:2505.07566* (2025).

52. U. S. Kamilov, C. A. Bouman, G. T. Buzzard, B. Wohlberg, Plug-and-play methods for integrating physical and learned models in computational imaging: Theory, algorithms, and applications. *IEEE Signal Process. Mag.* **40**, 85–97 (2023).
53. K. C. Tam, V. Perez-Mendez, Tomographical imaging with limited-angle input. *J. Opt. Soc. Am.* **71**, 582 (1981).
54. B. E. Treeby, B. T. Cox, k-wave: Matlab toolbox for the simulation and reconstruction of photoacoustic wave fields. *J. Biomed. Opt.* **15**, 021314–021314 (2010).

Acknowledgments

We wish to thank F. Bureau for fruitful discussions on the method and its applications as well as for providing the ultrasound data of the 3D experiment. We also wish to thank the authors of (32) for publishing in open-access the experimental ultrasound data used for the 2D in vitro experiment.

Funding: The authors are grateful for the funding provided by Labex WIFI (Laboratory of Excellence within the French Program Investments for the Future; ANR-10-LABX-24 and ANR-10-IDEX-0001-02 PSL*). This project has also received funding from the European Research Council (ERC) under the European Union’s Horizon 2020 research and innovation program (grant agreement no. 610110, REMINISCENCE project, A.A.). E.B. acknowledges financial support from the SuperSonic Imagine company.

Author contributions: B.H.-D. and A.A. initiated the project. B.H.-D. and A.A. conceived the method. B.H.-D and A.A. developed the theoretical background. E.B. developed the implementation of the split step Fourier method. B.H.-D. implemented the differential matrix imaging process. F.C conducted the clinical experiment. E.B. and W.L. gathered and processed the clinical ultrasound data. B.R. adapted the method to this configuration. B.H.-D. and A.A. prepared the manuscript. B.H.-D., E.B., B.R., W.L., F.C., M.F. and A.A. contributed to the discussion of the results and the development of the manuscript.

Competing interests: B.H.-D., M.F. and A.A. are inventors on a patent related to this work (no. FR2510672, filed in September 2025). E.B. and W.L. were employees of the SuperSonic Imagine company. All authors declare that they have no other competing interests.

Data and materials availability: 3D ultrasound data is available at Zenodo (<https://doi.org/10.5281/zenodo.8159177>).

Supplementary materials

Materials and Methods

Supplementary Text

Figs. S1 to S3

Table S1

Legends for Movies S1 to S7

References

Movies S1 to S7

Supplementary Materials for Physics-Based Learning of the Wave Speed Landscape in Complex Media.

Baptiste Hériard-Dubreuil*, Emma Brenner, Benjamin Rio, William Lambert,

Foucauld Channing's, Mathias Fink, Alexandre Aubry*

*Corresponding authors. Email: baptiste.heriard-dubreuil@espci.fr, alexandre.aubry@espci.fr

This PDF file includes:

Materials and Methods

Supplementary Text

Figures S1 to S3

Table S1

Legends for Movies S1 to S7

References

Materials and Methods

In this section, we describe in details the method presented in Figure 1, with a focus on the matrix imaging framework, the chosen numerical focusing algorithm (split-step Fourier method), the gradient implementation, the optimization techniques and the parameters used for the three experiments corresponding to Figures 3-5.

The following theoretical development will be performed in the case of ultrasound imaging but can be adapted to other reflection wave imaging configurations, as done previously with matrix imaging.

Matrix imaging, Numerical Focusing and Focusing quality

To perform an ultrasound acquisition, an ultrasonic probe emits a set of incident waves (\mathbf{i}) in the medium of interest. For each emission, the time-dependent back-scattered wave-field $\mathcal{R}(\mathbf{i}_{\text{in}}, \mathbf{o}_{\text{out}}, t)$ is recorded in a reception basis (\mathbf{o}). All recorded wave-fields are stored in a reflection matrix $\mathbf{R}_{io}(t) = [\mathcal{R}(\mathbf{i}_{\text{in}}, \mathbf{o}_{\text{out}}, t)]$. The simplest acquisition sequence is to emit with one element at a time and for each emission record with all elements the time-dependent field reflected back from the medium. In this case, the reflection matrix $\mathbf{R}_{uu}(t)$ is therefore recorded in the transducer basis (\mathbf{u}) and its elements $\mathcal{R}(\mathbf{u}_{\text{in}}, \mathbf{u}_{\text{out}}, t)$ correspond to the impulse response between each transducer. This canonical basis is the one used in the numerical simulation described further and in the in vitro experiment (32) whose ultrasound data set has been used for the first experimental proof-of-concept described in the accompanying paper (Fig. 3). Alternately, the reflection matrix can be acquired using beam forming (emitting and/or receiving with all elements in concert with appropriate time delays applied to each element) to form, for example, focused beams as in the conventional B-mode or plane waves of incident angle α for high frame rate imaging (44). This plane wave basis (α) was actually used as an emission basis ($\mathbf{i} = \alpha$) to record the reflection matrix $\mathbf{R}_{\alpha u}(t)$ for the in-vivo breast data (Fig. 5) processed in the accompanying paper.

To numerically focus the acquired signals at a given point in the medium, usual imaging techniques model the propagation of emitted and received waves and apply their time-reversed counterparts to the reflection matrix $\mathbf{R}_{io}(t)$. Such an operation is denoted as time-reversal, back-projection, adjoint imaging or migration in the different fields of wave physics. In this paper, this

focusing operation is performed in the frequency domain by considering the transmission matrix $\mathbf{T}_{ri}(f; c) = [\mathcal{T}(\mathbf{r}_{in}, \mathbf{i}_{in}, f; c)]$ that links, at each frequency f and according to the velocity model c , the emission basis (\mathbf{i}) to the focused basis (\mathbf{r}) that contains a set of focusing points \mathbf{r}_{in} inside the medium under study. Each column of the transmission matrix corresponds to the incident wave-field at each point \mathbf{r}_{in} induced by each emitted wave \mathbf{i}_{in} for a wave velocity model c .

This transmission matrix depends on the chosen propagation model and is of the upmost importance for the numerical focusing process. Its expression in the case of an advanced propagation model (split-step Fourier method) will be discussed in details in the next section. In the simple case of a homogeneous velocity model $c(\mathbf{r}) = c_0$ for all \mathbf{r} , its expression can be found analytically from the homogeneous wave equation. For instance, for a point-like emission at position \mathbf{u}_{in} , we obtain the Green's functions of the wave equation in 2D:

$$\mathcal{T}(\mathbf{r}_{in}, \mathbf{u}_{in}, f; c_0) = -\frac{j}{4} \mathcal{H}_0^{(1)}(k_0 |\mathbf{u}_{in} - \mathbf{r}_{in}|), \quad (S1)$$

with $k_0 = 2\pi f/c_0$ the wavenumber and $\mathcal{H}_0^{(1)}(-)$ the Hankel function of the first kind. Similarly, for a plane wave emission of propagation angle α_{in} in 2D, we have:

$$\mathcal{T}(\mathbf{r}_{in}, \alpha_{in}, f; c_0) = \exp \left[j k_0 \begin{pmatrix} \sin \alpha_{in} \\ \cos \alpha_{in} \end{pmatrix} \cdot \mathbf{r}_{in} \right], \quad (S2)$$

with \cdot the scalar product and $j = \sqrt{-1}$ the unitary imaginary number. As per the emission case, we can define a reception transmission matrix $\mathbf{T}_{ro}(f; c) = [\mathcal{T}(\mathbf{r}_{out}, \mathbf{o}_{out}, f; c)]$, between the reception basis (\mathbf{o}) and the focused basis (\mathbf{r}) .

To perform the numerical focusing, we multiply the time-reversed counterpart of the transmission responses \mathcal{T} (i.e. their complex conjugates in the Fourier domain) with each frequency component $\mathcal{R}(\mathbf{i}_{in}, \mathbf{o}_{out}, f)$ of the acquired reflection matrix. A sum over all emissions and receptions allows us to perform transmit and receive focusing operations in post-processing. A sum over frequency amounts to time gate the backscattered signal at an echo time fixed by the wave velocity model. We finally obtain a reflection (confocal) image $\mathcal{I}(\mathbf{r}; c)$ for any position \mathbf{r} :

$$\mathcal{I}(\mathbf{r}; c) = \sum_f \sum_{\substack{\mathbf{i}_{in} \in \mathbf{i} \\ \mathbf{o}_{out} \in \mathbf{o}}} \mathcal{T}^*(\mathbf{r}, \mathbf{i}_{in}, f; c) \mathcal{R}(\mathbf{i}_{in}, \mathbf{o}_{out}, f) \mathcal{T}^*(\mathbf{r}, \mathbf{o}_{out}, f; c). \quad (S3)$$

where the symbol $*$ stands for phase conjugate.

The matrix imaging framework goes beyond traditional confocal imaging as it separates the focusing points in emission and reception. In practice, it consists in considering different focal spots \mathbf{r}_{in} and \mathbf{r}_{out} in the transmission functions \mathcal{T} :

$$\bar{\mathcal{R}}(\mathbf{r}_{in}, \mathbf{r}_{out}; c) = \sum_f \sum_{\substack{\mathbf{i}_{in} \in \mathcal{I} \\ \mathbf{o}_{out} \in \mathcal{O}}} \mathcal{T}^*(\mathbf{r}_{in}, \mathbf{i}_{in}, f; c) \mathcal{R}(\mathbf{i}_{in}, \mathbf{o}_{out}, f) \mathcal{T}^*(\mathbf{r}_{out}, \mathbf{o}_{out}, f; c), \quad (S4)$$

or, under a matrix formalism,

$$\bar{\mathbf{R}}_{rr}(c) = \sum_f \mathbf{T}_{ri}^*(f; c) \times \mathbf{R}_{io}(f) \times \mathbf{T}_{ro}^\dagger(f; c). \quad (S5)$$

with \dagger the hermitian transpose operation and \times the matrix product. The time-gated focused reflection matrix $\bar{\mathbf{R}}_{rr} = [\bar{\mathcal{R}}(\mathbf{r}_{in}, \mathbf{r}_{out}; c)]$ contains the cross-talks between the emission and reception focusing points that act as virtual sources \mathbf{r}_{in} and receivers \mathbf{r}_{out} . When the emission and reception focal points coincide ($\mathbf{r}_{in} = \mathbf{r}_{out}$), we fall back to the confocal image \mathcal{I} . The confocal image actually corresponds to the diagonal coefficients of $\bar{\mathbf{R}}_{rr}$:

$$\mathcal{I}(\mathbf{r}; c) = \bar{\mathcal{R}}(\mathbf{r}, \mathbf{r}; c) = \text{diag}(\bar{\mathbf{R}}_{rr}(c)). \quad (S6)$$

In practice, we can restrict our study to pairs of virtual transducers, $\mathbf{r}_{in} = (\mathbf{x}_{in}, z)$ and $\mathbf{r}_{out} = (\mathbf{x}_{out}, z)$, located at the same depth z . A focused sub-matrix $\bar{\mathbf{R}}_{xx}(z; c) = [\bar{\mathcal{R}}(\mathbf{x}_{in}, \mathbf{x}_{out}, z; c)]$ can then be considered at each depth z :

$$\bar{\mathbf{R}}_{xx}(z; c) = \sum_f \mathbf{T}_{xi}^*(z, f; c) \times \mathbf{R}_{io}(f) \times \mathbf{T}_{xo}^\dagger(z, f; c), \quad (S7)$$

Similarly to the full focused reflection matrix $\bar{\mathbf{R}}_{rr}(c)$ (Eq. S6), the diagonal of each sub-matrix $\bar{\mathbf{R}}_{xx}(z; c)$ corresponds to the confocal reflection image at depth z .

The focused reflection matrix provides a self-portrait of the focusing process and have been studied for multiple applications such as ultrasound imaging (17, 16), optical coherence microscopy (45) or passive seismic imaging (41). In particular, it can be used to assess the numerical focusing efficiency as the width of its diagonal is representative of the effective size of the focal spots. The profile along the antidiagonal of the focused reflection matrices is called the reflection point-spread-function or RPSF (17). More specifically, echoes that have been successfully focused lie on the diagonal of the focused reflection matrix whereas echoes resulting from aberrations or multiple

scattering, that are not adequately grasped by the forward model and/or not correctly inverted by the focusing process, spread outside of diagonal. We devise a focusing quality criterion by averaging the energy on the diagonal of the focused reflection matrix, normalized by the energy averaged over each column of the focused reflection matrix:

$$\mathcal{F}(c) = \left\langle \frac{|\bar{\mathcal{R}}(\mathbf{x}, \mathbf{x}, z; c)|^2}{\sum_{\mathbf{x}'} |\bar{\mathcal{R}}(\mathbf{x}', \mathbf{x}, z; c)|^2} \right\rangle_{\mathbf{x}, z}, \quad (S8)$$

where \mathbf{x} represents the lateral coordinates [x in 2D and (x, y) in 3D]. This criterion is representative of the diagonal feature of the focused reflection matrix and therefore of the efficiency of the numerical focusing process.

To improve the robustness of this focusing quality criterion, especially for large domains or *in vivo* configurations, we apply a confocal filter to the focused reflection matrix before computing the quality criterion. This confocal filter decreases the contribution of random multiple scattering trajectories that give rise to a drastic off-diagonal spreading of the RPSF and that can not be grasped by our forward model. For a confocal filter of width w (typically a few tens of the wavelength λ), we obtain a filtered focused reflection matrix $\bar{\mathcal{R}}_{\mathbf{x}\mathbf{x}}(z; c)$ defined as:

$$\bar{\mathcal{R}}(\mathbf{x}_{in}, \mathbf{x}_{out}, z; c) = \begin{cases} \bar{\mathcal{R}}(\mathbf{x}_{in}, \mathbf{x}_{out}, z; c) & \text{if } |\mathbf{x}_{in} - \mathbf{x}_{out}| < w, \\ 0 & \text{else.} \end{cases} \quad (S9)$$

With this matrix imaging framework, numerical focusing and the quality factor can be used equivalently in 2D or 3D configurations. In the latter case, the position \mathbf{r} corresponds to three coordinates (x, y, z) and the focused reflection matrices are four-dimensional.

The Split-Step Fourier Method

The modeling of the transmission matrices, $\mathbf{T}_{ri}(f; c)$ and $\mathbf{T}_{ro}(f; c)$, is crucial to reach a satisfying focusing process in heterogeneous media. On one hand, it needs to be sufficiently simple so that the optimization process is tractable. On the other hand, it needs to be accurate enough to focus efficiently in complex media. State of the art solutions use drastic assumptions on wave propagation to simplify the transmission matrix. For instance, wave propagation can be modeled as a straight way propagation (46, 20) or as a propagation in a homogeneous medium with one or several phase screens (17, 16, 47). In our case, we want to address highly heterogeneous media and therefore

choose a propagation model that takes into account advanced wave propagation phenomena such as refraction and forward multiple scattering. To do so, we use the split-step Fourier method (25), also called the beam propagation method in optics (27). This method models wave propagation as a succession of phase screens and free-field propagation at the wavelength level, and approximates accurately the wave equation solution when the wave propagates in a preferred direction.

The implementation of the split-step Fourier method starts with an interpolation whose goal is to express the experimental reflection matrices $\mathbf{R}_{io}(f)$ as a set of focused reflection matrices $\mathbf{R}_{xx}(z_0, f)$ on a starting plane $z = z_0$ for all frequencies. In practice, we often choose the starting plane to be the sensor plane, defined as $z_0 = 0$ in the rest of this chapter. We use either a spatial interpolation if emissions or receptions are performed in the transducer basis, or an inverse Fourier transforms in the case of plane wave emissions. For less ordinary emissions or receptions, such interpolation can be a transmission matrix in itself, representing the propagation between the emission (or reception) basis to the plane $z = 0$. We denote this interpolation operator as a matrix $\mathbf{I}_{xi}(f)$ (respectively $\mathbf{I}_{xo}(f)$ for the reception side), leading to the following formula:

$$\mathbf{R}_{xx}(0, f; c) = \mathbf{I}_{xi}(f; c) \times \mathbf{R}_{io}(f) \times \mathbf{I}_{xo}^T(f; c). \quad (\text{S10})$$

In standard cases (transducer or plane wave emission and reception bases), it is possible to write such an interpolation in a way that does not depend on the wave velocity model. In more uncommon cases, this operator may depend on a wave velocity hypothesis.

With the obtained focused reflection matrices $\mathbf{R}_{xx}(0, f)$ at plane $z = 0$ and for each frequency f , we decompose the transmission function as a series of elementary operators that model the propagation in a slice of height δz . These elementary operators depend on the wave velocity model at depth z denoted as $c(z)$ and are written $\delta\mathbf{T}_{xx}(\delta z, f; c(z))$. We obtain for the propagation between planes z and $z + \delta z$:

$$\mathbf{R}(z + \delta z, f; c) = \delta\mathbf{T}^*(\delta z, f; c(z)) \times \mathbf{R}(z, f; c) \times \delta\mathbf{T}^\dagger(\delta z, f; c(z)), \quad (\text{S11})$$

where all subscripts $-_{xx}$ have been removed for the sake of simplicity. The elementary operator $\delta\mathbf{T}$ is defined as a free-space propagation performed in the frequency domain followed by a phase screen modeling the lateral variations of the wave velocity:

$$\delta\mathbf{T}(\delta z, f; c(z)) = \mathbf{s}(f; c(z)) \odot \left(\mathbf{F}^\dagger \times (\mathbf{h}(f, c(z)) \odot \mathbf{F}) \right), \quad (\text{S12})$$

where the symbol \odot stands for the Hadamard (element wise) product. $\mathbf{F} = [F(\mathbf{f}_x, \mathbf{x})]$ is the spatial Fourier transform (implemented with the fast Fourier transform in practice), such that:

$$F(\mathbf{f}_x, \mathbf{x}) = \exp(-j2\pi \mathbf{f}_x \cdot \mathbf{x}), \quad (S13)$$

with \mathbf{f}_x the lateral spatial frequencies, written as a vector. $\mathbf{h}(f, c_m(z)) = [h(\mathbf{f}_x, f, c_m(z))]$ is the free-space propagation operator over depth δz defined for a constant wave speed $c_m(z)$. $\mathbf{s}(f; c(z)) = [s(\mathbf{x}, f; c(z))]$ is the phase screen operator defined in real space. In Eq. S12, all upper case bold letters represent matrices and all lower case bold letters represent vectors. The propagation operator \mathbf{h} and the phase screen \mathbf{s} can be expressed as a function of the slowness, defined as the inverse of the velocity, $\sigma(\mathbf{x}, z) = 1/c(\mathbf{x}, z)$. More precisely, \mathbf{h} is dictated by the average slowness $\sigma_m(z) = \langle \sigma(\mathbf{x}, z) \rangle_x = 1/c_m(z)$ and \mathbf{s} by its residual $\delta\sigma(\mathbf{x}, z) = \sigma(\mathbf{x}, z) - \sigma_m(z)$ at depth z , such that:

$$\mathbf{h}(f, c(z)) = \exp\left(j2\pi\delta z \sqrt{(f\sigma_m(z))^2 - |\mathbf{f}_x|^2}\right), \quad (S14)$$

$$\mathbf{s}(f, c(z)) = \exp(j2\pi\delta z f \delta\sigma(\mathbf{x}, z)), \quad (S15)$$

with $\sqrt{-}$ the complex square root.

The free-space propagation is performed in the spatial Fourier space which supposes periodic boundaries. In practice, we prefer to consider absorbing boundaries that can be implemented using a lateral padding and adding an apodization step at the end of the elementary propagation (S11). This apodization is performed by multiplying the result of the propagation by a function equal to 1 in the domain of interest, and decreasing to 0 continuously in the padding section (e.g. using a Tukey window).

With this recursive implicit definition of the transmission matrix, the experimental reflection matrix is first projected on plane $z = 0$ with (S10) and then propagated iteratively at all depths with (S11). At each depth, the obtained focused reflection matrices can be summed over temporal frequencies to perform time-gating and compute the focusing quality (S8).

Factorization

The computation of the focused reflection matrix at each depth can be computationally expensive and requires a large amount of memory. This is particularly the case for the 3D configuration

where the presence of two lateral dimensions leads to 4D focused reflection matrices. The most expensive operation is the iteration of (S11). It can be implemented without any matrix multiplications using only separable fast Fourier transforms and element-wise multiplications, leading to an overall computation cost at each depth for each frequency in the order of $O(N_x^2 \log N_x)$ in 2D and $O(N_x^2 N_y^2 \log N_x)$ in 3D (taking $N_x > N_y$ without loss of generality).

In ultrasound imaging, the number of emissions is usually significantly lower than the number of lateral positions $N_i \ll N_x$. To leverage this property, we replace focused reflection matrices of size $N_x \times N_x$ by two matrices of size $N_i \times N_x$ (for each depth and each frequency). These two matrices, denoted as $\mathbf{T}_{ix}(z, f; c)$ and $\mathbf{R}_{ix}(z, f; c)$, correspond to the emission part and the reception part of the focused reflection matrices. They can be computed recursively in a similar way as the focused reflection matrices. Initialization is performed using the interpolation matrices as in (S10):

$$\begin{cases} \mathbf{T}_{ix}(0, f; c) = \mathbf{I}_{xi}^\dagger(f; c), \\ \mathbf{R}_{ix}(0, f; c) = \mathbf{R}_{io}(f) \times \mathbf{I}_{xo}^T(f; c). \end{cases} \quad (\text{S16})$$

Their propagation from depth z to $z + \delta z$ is performed with the following update formulae:

$$\begin{cases} \mathbf{T}_{ix}(z + dz, f; c) = \mathbf{T}_{ix}(z, f; c) \times \delta \mathbf{T}_{xi}^T(\delta z, f; c(z)), \\ \mathbf{R}_{ix}(z + dz, f; c) = \mathbf{R}_{ix}(z, f; c) \times \delta \mathbf{T}_{xi}^\dagger(\delta z, f; c(z)). \end{cases} \quad (\text{S17})$$

With this representation, we can recover the focused reflection matrices at each depth:

$$\mathbf{R}_{xx}(z, f; c) = \mathbf{T}_{ix}^\dagger(z, f; c) \times \mathbf{R}_{ix}(z, f; c). \quad (\text{S18})$$

These two matrices therefore contain all the information of the focused reflection matrices but are computationally significantly cheaper due to their reduced size. They result in a computation cost at each depth for each frequency of $O(N_i N_x \log N_x)$ in 2D and $O(N_i N_x N_y \log N_x)$ in 3D. However, the matrix multiplication of (S18) is expensive and becomes the bottleneck of our algorithm. To circumvent this issue, we rather work with the distortion matrix (48), obtained by element-wise multiplication of our two matrices:

$$\mathbf{D}_{ix}(z, f; c) = \mathbf{T}_{ix}^*(z, f; c) \odot \mathbf{R}_{ix}(z, f; c). \quad (\text{S19})$$

One can notice that the diagonal of the focused reflection matrix, equal to the confocal reflectivity

image, can be recovered directly from the distortion matrix by summing its rows:

$$\mathbf{I}(z; c) = \sum_f \sum_i \mathbf{D}_{ix}(z, f; c). \quad (\text{S20})$$

As a result, we can compute the numerator of the focusing quality index without explicitly computing the focused reflection matrices. However, the denominator cannot be obtained without a large amount of multiplications. We use in practice an approximation of this denominator by computing the norm of the distortion matrix. The obtained focusing quality index $\tilde{\mathcal{F}}(c)$ resembles the focusing criterion introduced by Mallart et al. (49):

$$\tilde{\mathcal{F}}(c) = \left\langle \frac{|\sum_{f,i} \mathcal{D}(i, \mathbf{x}, z, f; c)|^2}{\sum_i |\sum_f \mathcal{D}(i, \mathbf{x}, f, z; c)|^2} \right\rangle_{\mathbf{x}, z}. \quad (\text{S21})$$

With this version of the quality factor, the focused reflection matrices is never explicitly computed and the computational complexity and memory footprint is therefore kept low.

This factorization results in a large gain in computation time and memory requirement, providing that the number of emissions is significantly lower than the number of lateral positions. In particular, this simplification is key to generalize to 3D configurations.

Differentiability and Gradient implementation

In the previous sections, we defined the operations applied to the raw data, given a velocity model, to obtain a focusing quality criterion. This forward model is represented in the upper row of Figure 1.

We now want to compute the gradient of the focusing quality factor with respect to the velocity model to perform an optimization, as represented in the lower row of Figure 1. This gradient can be computed using the chain rule as in equation (4). In more details, we obtain:

$$\frac{\partial \mathcal{F}}{\partial c} = \sum_{z,f} \frac{\partial \mathcal{F}}{\partial \mathbf{R}(z, f; c)} \sum_{z' \leq z} \frac{\partial \mathbf{R}(z, f; c)}{\partial \delta \mathbf{T}(\delta z, f; c(z'))} \frac{\partial \delta \mathbf{T}(\delta z, f; c(z'))}{\partial c}, \quad (\text{S22})$$

where the subscript $-_{xx}$ has been removed for the sake of clarity.

To compute these derivatives, we choose to implement the forward model in an auto-differentiable language (in our case, PyTorch), inspired by recent works in adaptive ultrasound imaging (46, 50, 47, 20). With such a language, the chain rule is performed automatically. Nevertheless, the study of the differentiability of all operators and of their derivatives is crucial for a robust and efficient

optimization. In our case, the most complex operation is the computation of $\delta\mathbf{T}$ which depends on the wave velocity c via the two vectors \mathbf{h} and \mathbf{s} , as detailed in (S14) and (S15). In these two equations, vectors \mathbf{h} and \mathbf{s} depend on the slowness $\sigma = 1/c$ rather than the wave speed c . We therefore choose to optimize the focusing quality with respect to the slowness rather than the wave velocity. In addition, the expression \mathbf{h} is the only non-differentiable operation as it involves a complex square root which can be null for some frequencies. To remove the singularity at zero and bound the derivative of our model, we modify the formula of \mathbf{h} to include a small complex offset, resulting in a smooth expression in the complex plane:

$$\tilde{\mathbf{h}}(f, c(z)) = \exp \left(j2\pi\delta z \sqrt{(f\sigma_m(z))^2 - |f_x|^2 + j\epsilon} \right), \quad (\text{S23})$$

with ϵ a small positive real number, usually set to $\epsilon = |df_x|^2$ with df_x the spatial frequency step.

Finally, the gradient computation requires a large amount of memory, mainly due to the first two terms of (S22). Indeed, the focusing quality depends on all the focused reflection matrices (i.e. for all depths and frequencies), which themselves depend on all previous elementary transmission operators $\delta\mathbf{T}(\delta z, f; c(z'))$ for $z' < z$. Even with a clever implementation, this gradient computation requires to store all reflection matrices (or equivalently all elementary transmission matrices) as intermediate values. To limit the memory footprint of the gradient, we separate its computation into a first part where frequencies are handled independently, and a second part that mixes the frequencies. We compute the gradient of the first part by batching on the frequencies, and combine all results with the second part. This strategy gives a new parameter (the batch size) which controls the trade-off between computation efficiency and memory management.

Optimization Problem and Convergence

The proposed forward model, which computes focusing quality as a function of the wave slowness map, is non-linear and likely ill-posed. There is no theoretical guarantees on the convergence of the gradient ascent algorithm nor on the fact that the global maximum of the focusing quality factor is associated with the actual slowness map. Such a guarantee exists for homogeneous media (51) but has not been demonstrated for heterogeneous media yet. Nevertheless, we can study the convergence of the gradient ascent algorithm from an empirical standpoint.

We start by solving the following optimization problem:

$$\max_{\sigma} \mathcal{F}(\sigma), \quad (\text{S24})$$

with σ the slowness map. We perform a naive gradient ascent algorithm which iteration step consists in updating the slowness as $\sigma \leftarrow \sigma + \epsilon \nabla_{\sigma} \mathcal{F}(\sigma)$, with ϵ a learning rate. In practice, the gradient ascent algorithm is implemented with an Adam optimizer.

We apply this algorithm on a simulation of a heterogeneous medium. The result shows high short-scale spatial variations, as represented in Figure S1.A. These variations do not correspond to any physical reality and are interpreted as overfitting. Since we seek to recover the large-scale variations of the wave velocity, we introduce a smoothness prior in the form of a regularization to mitigate such variations:

$$\max_{\sigma} \mathcal{F}(\sigma) + \eta TV(\sigma), \quad (\text{S25})$$

with $TV(\sigma) = \langle \|\nabla \sigma\|_1 \rangle_{x,z}$ a total variation regularization implemented in its anisotropic ℓ -1 version and η a regularization weight. The result is displayed in Figure S1.B. and shows a drastic reduction of noise in the velocity map. However, a few short-scale spatial variations remain. Such artifacts are particularly stable as they are often associated with delays of exactly one or several cycles of the emitted pulse. They are described as cycle skipping artifacts in the tomography literature and correspond to phase interference of waves. To avoid this pitfall without enforcing an unreasonable smoothness prior on the slowness map, we perform a median filtering step at each iteration on the result of the gradient ascent. The gradient ascent steps becomes $\sigma \leftarrow f(\sigma + \epsilon(\nabla_{\sigma} \mathcal{F}(\sigma) + \eta \nabla_{\sigma} TV(\sigma)))$, where f is a partial median filer defined as:

$$f(\sigma) = \alpha \cdot \sigma + (1 - \alpha) \cdot m(\sigma), \quad (\text{S26})$$

with $m(-)$ a median filtering operator and α a small constant usually set to $\alpha = 0.5$. This filtering step can be interpreted as a denoising operation similar to the implicit proximal of plug and play algorithms (52). It results in an accurate speed-of-sound estimator (see Figure S1) and accelerates the overall convergence.

If the regularization and the filtering step solve most convergence issues, an asymmetry of the forward problem remains. Indeed, the focusing quality is affected by phase aberrations accumulated during wave propagation. This accumulation corresponds to axial integrals of the slowness map,

resulting in difficulties to recover the high-frequency axial variations of the wave velocity. This limitation is linked to the so-called missing cone problem in tomography (53). In our case, the computation of the focusing quality at all depths and the presence of scattering and refraction effects mitigate the missing cone problem and enables us to accurately recover an axial profile. However, this asymmetry still leads to a slow axial convergence compared to the estimation of lateral variations. As a result, our algorithm tends to compensate axial velocity variations by creating an artificial lateral profile, as shown in Figure S2.B. The mathematical origin of this effect takes its roots in the split-step Fourier algorithm in which the wave slowness is separated into an axial profile term σ_m used for the free-space propagation in (S14) and a residual lateral term $\delta\sigma$ used as a phase mask in (S15). This separation may result in contrary gradient directions which hinder the convergence. To circumvent this issue, we separate the slowness into two different variables σ_m and $\delta\sigma$, used for the free space propagations (S14) and the phase screens (S15) respectively. Our optimization problem becomes:

$$\begin{aligned} \max_{\delta\sigma, \sigma_m} \quad & \mathcal{F}(\delta\sigma, \sigma_m) + \eta TV(\delta\sigma, \sigma_m), \\ \text{such that} \quad & \langle \delta\sigma \rangle_x = 0. \end{aligned} \quad (S27)$$

In this form, the constraint may still block the gradient ascent. We perform a Lagrangian relaxation of this constraint to resolve the conflict:

$$\max_{\delta\sigma, \sigma_m} \mathcal{F}(\delta\sigma, \sigma_m) + \eta TV(\delta\sigma, \sigma_m) + \mu \|\langle \delta\sigma \rangle_x\|, \quad (S28)$$

where $\| - \|$ can be any norm. In our case, we take $\mu = 0$, leading to a loss similar to the one of equation (S25), but optimized on two independent variables. Such a relaxation can be interpreted as a dimension increase that facilitates the convergence.

Finally, we adapt the gradient ascent by considering two optimization phases. In the first phase, we only optimize the axial profile σ_m . In the second phase, we start from the result of the first phase and optimize jointly the two variables. The variable splitting combined with this adapted ascent algorithm results in an accurate estimation of both the axial profile of the wave velocity and its lateral variations, as seen in Figure S2.C.

Experimental Parameters

We here present the parameters used for the three experiments corresponding to Figures 3, 4, 5 as well as the simulation validation presented in the Supplementary text in Figure S3.

All parameters are reported in Table S1. Due to the need for application-specific ultrasound hardware, probes and emission parameters vary between the experiments. The 2D *in vitro* acquisition was performed with a Verasonics Vantage 256 scanner (Verasonics Inc., Kirkland, WA, USA) using a L12-5 ultrasound probe. The 3D *in vitro* experiment was performed with a 2D matrix array of transducers (Vermon) using an electronic hardware developed by Supersonic Imagine (Aix-en-Provence, France). The clinical acquisition was performed with a Mach 30 scanner (Supersonic Imagine, Aix-en-Provence, France).

Due to differences in the acquisition setup, we adapt the grid size for each experiment. The grid resolution can be chosen arbitrarily between half a wavelength and two wavelengths and constitutes a trade-off between reconstruction accuracy and computation time. We choose 0.8 wavelengths for the 2D configurations and one wavelength for the 3D case, the considered wavelength being estimated at the central frequency. This grid is used both for the velocity model and quality factor computation. The initial velocity model is always chosen homogeneous, with a value that corresponds to the expected average value (e.g. 1480 m.s^{-1} or 1540 m.s^{-1}). A variation of the initial velocity does not result in a bias (for reasonable variations, i.e lower than 10%) but may lead to increased convergence time and spatial instabilities. The factorization presented in (S16) and (S17) is always used as the number of emissions is always smaller than the number of lateral points in the grid. In the 3D case, we even use the distortion matrix representation presented in (S21) in order not to compute explicitly the reflection matrix which would be of size $60 \times 40 \times 60 \times 40$ for each depth and frequency (i.e. several hundreds of billions of values).

Finally, the optimization parameters are fine tuned empirically for each configuration. The number of iterations is set to 100 for each phase of the convergence process (axial and lateral), with an early stopping criterion based on the average evolution of the loss in 10 consecutive iterations.

In the clinical case, the long probe and shallow depths of imaging result in an unusual geometry with a width over height ratio of 1.7. In this case, the decomposition of the slowness map as an axial profile plus a lateral residual slowness shows limitations. To recover a configuration similar to the

other cases, we decompose our medium into three overlapping columns 125 wavelengths wide, and perform the optimization on these three columns independently. A final optimization is performed on the full domain, with the result of the previous optimizations used as the initial velocity model.

Supplementary Text

Simulation Validation

We validate the proposed method using simulations performed with k-Wave (54). Simulation parameters are reported in Table S1 and results are displayed in Figure S3.

For each simulation, we define a wave velocity map made of large scale variations such as inclusions or layers, and a density map containing short scale variations such as sub-wavelength scatterers and anechoic regions. We simulate ultrasound acquisitions in such media, and apply the proposed method to the resulting signals. The optimization is performed on one NVIDIA RTX 6000 Ada Generation GPU, converging in 1 to 35 minutes (depending on the grid size).

We display in Fig. S3 the aberrated reflection images obtained with a uniform wave velocity hypothesis of 1540 m.s^{-1} and compare it with the reflection image obtained at convergence. In all cases, a sharp reflection image is recovered without any geometric distortions, which validates the ability to correct aberrations with the proposed method. The estimated wave velocity map is compared to the simulated one on the right part of Figure S3. In the three first simulations, we obtain an accurate velocity estimate with a high lateral resolution (approximately one wavelength) and an axial resolution of a few wavelengths. This asymmetric resolution is a direct manifestation of the missing cone problem even though it is here partially mitigated by refraction and scattering. Obtained velocity values are close to the ground truth, with absolute errors lower than 20 m.s^{-1} .

The last simulation models a more complex configuration. In this case, we observe a good agreement between the estimated and ground truth value in the center of the domain. However, we observe some lateral border effects as well as a low accuracy at high depths. These limitations can be explained by the low impact of the velocity values at such positions on the average focusing quality. For future applications, results could be improved by masking or correcting such border effects.

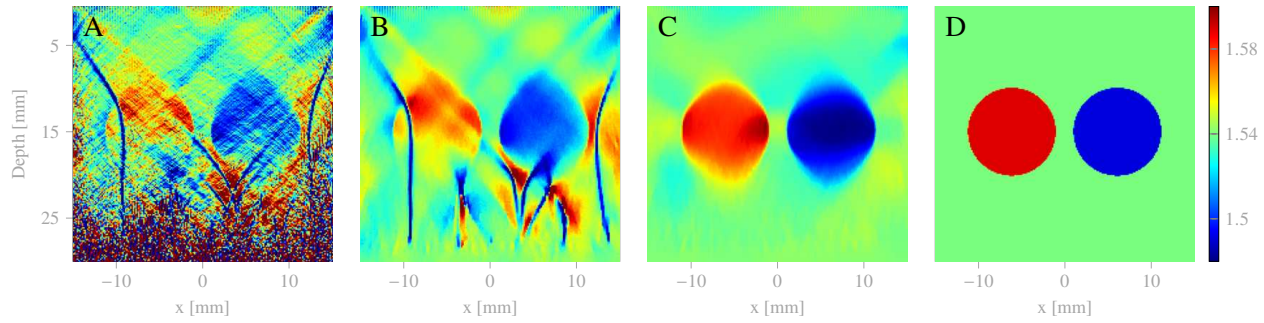


Figure S1: Effect of regularization and filtering on the convergence. Wave velocity maps at convergence for an ultrasound simulation. **(A)** Result without regularization nor filtering. **(B)** Result with regularization but without filtering. **(C)** Result with regularization and filtering. **(D)** Ground truth. All speed of sound values are given in $\text{mm}.\mu\text{s}^{-1}$.

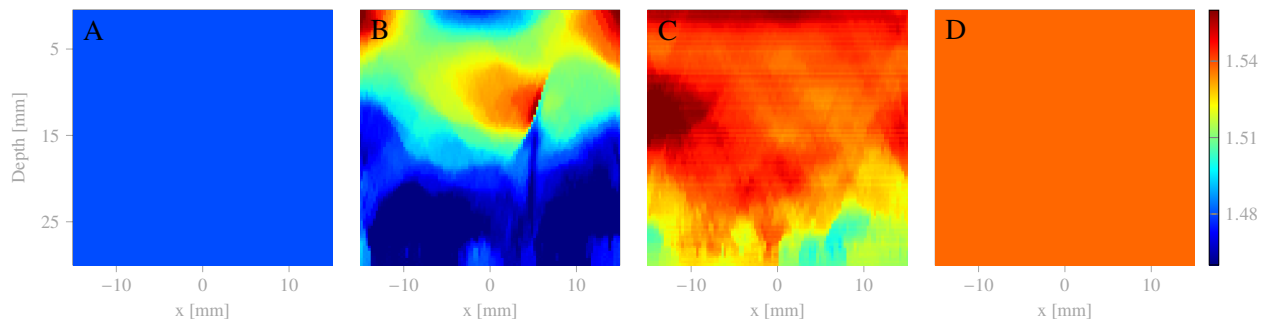


Figure S2: Effect of variable splitting on the convergence. Wave velocity maps at convergence for an ultrasound simulation. **(A)** Initial hypothesis for the wave velocity. **(B)** Result without variable splitting. **(C)** Result with variable splitting. **(D)** Ground truth. All speed of sound values are given in $\text{mm}.\mu\text{s}^{-1}$.

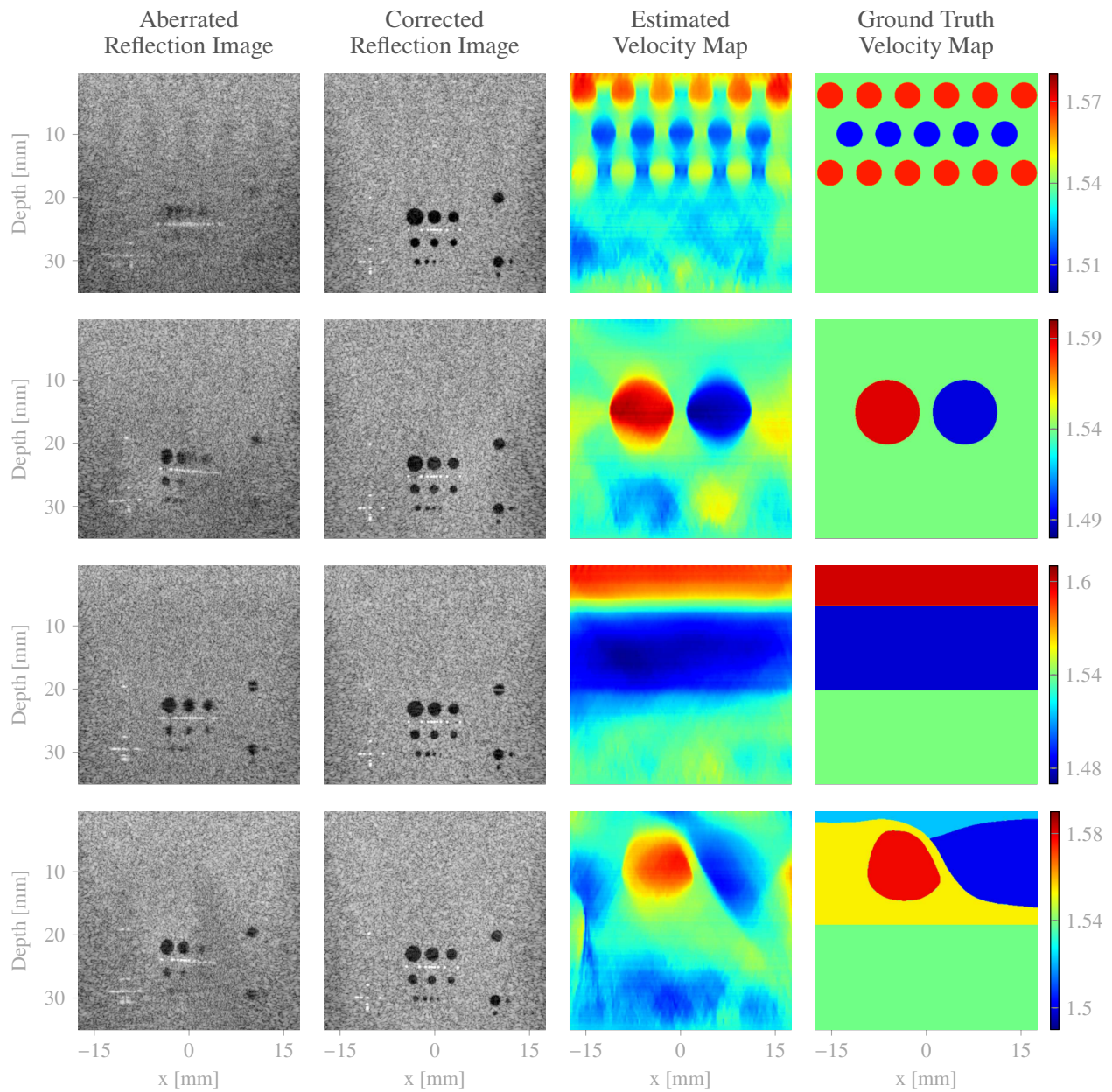


Figure S3: Simulation validation of the proposed method. Four different media are simulated using k-Wave with heterogeneous velocity maps displayed in the rightmost column. Resulting reflection images are aberrated, as seen in the leftmost column. The two central columns present the reflection image and the wave velocity map obtained at convergence. Reflection images are represented in dB and speed of sound values are given in $\text{mm}.\mu\text{s}^{-1}$.

Table S1: Experimental parameters. Acquisition parameters, spatial grid parameters, algorithm choices and optimization parameters for the four different experiments. 2D simulation correspond to Fig. S3, 2D in vitro to Fig. 3, 2D clinical to Fig. 5 and 3D in vitro to Fig. 4.

Parameter	2D Simulation	2D In vitro	2D Clinical	3D In vitro
Central frequency [in MHz]	5.2	6	5 or 6.5	3
Bandwidth [at -6 dB, in %]	58	50	60	66
Number of transducers	128	256	256	32×32
Pitch [in mm]	0.3	0.195	0.2	0.5
Emission basis	transducer	transducer	plane wave	transducer
Number of emissions	128	128	61	8×16
Lateral size w [in λ]	150	200	250	60×40
Axial size h [in λ]	150	175	150	120
Grid resolution [in λ]	0.8	0.8	0.8	1
Padding width	$w/4$	$w/4$	$w/4$	$(w/4) \times (w/4)$
Initial velocity [mm, μs^{-1}]	1.54	1.48	1.48	1.54
Factorization	Yes	Yes	Yes	Yes
Focusing Quality formula	(S8)	(S8)	(S8)	(S21)
Confocal filter width [in λ]	32	32	32	–
Learning rate for σ_m	$2 \cdot 10^{-3}$	$2 \cdot 10^{-3}$	$2 \cdot 10^{-3}$	$1 \cdot 10^{-3}$
Learning rate for $\delta\sigma$	$6 \cdot 10^{-3}$	$5 \cdot 10^{-3}$	$8 \cdot 10^{-3}$	$4 \cdot 10^{-3}$
Regularization weight (σ_m)	2	2	2	1
Regularization weight ($\delta\sigma$)	5	5	5	20
Median filter size [in λ]	12×7	12×7	12×7	$5 \times 5 \times 5$

Caption for Movie S1. Aberration compensation in the 2D *in vitro* experiment. The initial (red square) and corrected (green square) images (Fig. 3B and E, respectively) are alternatively displayed to highlight the benefit of the optimized speed-of-sound map (Fig. 3F) for the beamforming process and the resulting reflection image. The dynamic range of the B&W scale is of 50 dB.

Caption for Movie S2. Aberration compensation of *ex vivo* tissues in a 3D configuration. The initial (red square) and corrected (green square, Fig. 4B) images are alternatively displayed to highlight the benefit of the optimized speed-of-sound map (Fig. 4D) for the beamforming process and the resulting reflection image. The dynamic range of the B&W scale is of 80 dB.

Caption for Movie S3. Aberration compensation in the first breast tissue experiment. The initial (red square) and corrected (green square, Fig. 5B) images are alternatively displayed to highlight the benefit of the optimized speed-of-sound map (Fig. 5C) for the beamforming process and the resulting reflection image. The dynamic range of the B&W scale is of 55 dB.

Caption for Movie S4. Aberration compensation in the second breast tissue experiment. The initial (red square) and corrected (green square, Fig. 5D) images are alternatively displayed to highlight the benefit of the optimized speed-of-sound map (Fig. 5E) for the beamforming process and the resulting reflection image. The dynamic range of the B&W scale is of 55 dB.

Caption for Movie S5. Aberration compensation in the third breast tissue experiment. The initial (red square) and corrected (green square, Fig. 5F) images are alternatively displayed to highlight the benefit of the optimized speed-of-sound map (Fig. 5G) for the beamforming process and the resulting reflection image. The dynamic range of the B&W scale is of 55 dB.

Caption for Movie S6. Aberration compensation in the fourth breast tissue experiment. The initial (red square) and corrected (green square, Fig. 5H) images are alternatively displayed to highlight the benefit of the optimized speed-of-sound map (Fig. 5I) for the beamforming process and the resulting reflection image. The dynamic range of the B&W scale is of 55 dB.

Caption for Movie S7. Aberration compensation in the fifth breast tissue experiment. The initial (red square) and corrected (green square, Fig. 5J) images are alternatively displayed to highlight the benefit of the optimized speed-of-sound map (Fig. 5K) for the beamforming process and the resulting reflection image. The dynamic range of the B&W scale is of 55 dB.